Atomic Structure of Antiphase Nanodomains in Fe-Doped $SrTiO_3$ Films

Hongchu Du, Chun-Lin Jia, Joachim Mayer, Juri Barthel, Christian Lenser, and Regina Dittmann*

The atomic structure of antiphase nanodomains in Fe-doped $SrTiO_3$ films is revealed directly by aberration-corrected scanning transmission electron microscopy. In particular, the crystallographic translation vector between the antiphase nanodomains and the matrix is determined to be $a/2$ [0 1 1], distinct from $a/2$ [0 1 1] for the well-known Ruddlesden–Popper (RP) planar faults in perovskite structure. The antiphase boundaries lie mostly in the {1 0 0} planes and partially in the {1 1 0} planes. The atomic structure of the antiphase boundaries is found to consist of chains of edge-sharing TiO_6 octahedra implying a local Ti-enrichment, which is in strong contrast to local Sr-enrichment at the RP type antiphase boundaries.

1. Introduction

Perovskite oxides exhibit many interesting emergent properties, including high-temperature superconductivity,[1] colossal magnetoresistance,[2] interfacial 2D electron gas,[3] strain induced ferroelectricity,[4] and resistive switching phenomenon.[5] This has led to decisive progress in the growth of multicomponent oxide as thin films by pulsed-laser deposition (PLD) and molecular-beam epitaxy techniques for integrated device applications. $SrTiO_3$ is one of these perovskite oxides that has been extensively studied as a model material to understand the underlying mechanism of the defect associated effects, such as oxygen incorporation[6] and resistive switching phenomena,[7] for which a profound knowledge on microstructures of a large variety of defects is a prerequisite.

Previous studies have shown that extended defects in $SrTiO_3$ are closely correlated with a deviation from stoichiometry, which can be controlled by carefully chosen deposition parameters such as laser fluence using PLD growth method.[8–10] The well-known Ruddlesden–Popper (RP) planar faults are consistently observed in Sr-rich $SrTiO_3$ films.[11–13,8] A RP planar fault can be described as a crystallographic shear plane with a lattice translation vector $t = a/2$ [1 1 1], corresponding to the insertion of an additional SrO layer parallel to the {1 0 0} planes. In contrast to Sr-rich films, strongly Ti-rich films have been reported to form amorphous TiO_2 precipitates.[14] Inhomogeneous contrast observed in high-resolution (scanning) transmission electron microscopy (HR(S)TEM) images of moderate Ti-rich films have been attributed to point defect induced distortions.[11,15] However, the atomic structure of the extended defects have rarely been investigated in Ti- (or B-site atom-) rich $SrTiO_3$ films.[16]

In the present work we report on the atomic structure of extended defects in PLD grown Fe-doped $SrTiO_3$ films by aberration corrected high-angle annular dark-field (HAADF) scanning transmission electron microscopy (STEM) imaging. The aim of this work is to provide the atomic arrangement of these extended defects in $SrTiO_3$ films. The observed extended defects are antiphase nanodomains formed by a lattice translation vector of $a/2$ [0 1 1] with respect to the surrounding film. In strong contrast to the RP phase, the antiphase domain boundaries (APBs) appear to be composed of edge-sharing TiO_6 octahedra, which are commonly seen in TiO_2, such as anatase.

2. Results and Discussion

2.1. Identification of Antiphase Nanodomain

To obtain complete structural information by TEM, it is often necessary to image the specimen along different orientations. The films were imaged along three orientations, [0 1 0] (cross-section), [1 1 0] (cross-section), and [0 0 1] (plan-view). **Figure 1** shows the representative cross-section and plan-view bright field TEM (BF-TEM) images of the film, in which randomly distributed dot clusters with a dark contrast show a size up to a few nanometers. The observed dark clusters are quite similar to the results reported in the literature,[11,15] which have been attributed to point defect-induced distortions.

In contrast to previous studies,[11,14,15] atomic resolution HAADF-STEM imaging provides evidence that the dark clusters observed in this work appear to be antiphase nanodomains.

Dr. H. Du, Prof. C.-L. Jia, Prof. J. Mayer, Dr. J. Barthel
Ernst Ruska-Centre for Microscopy and
Spectroscopy with Electrons
Jülich Research Centre
Jülich 52425, Germany
E-mail: h.du@fz-juelich.de

Dr. H. Du, Prof. J. Mayer, Dr. J. Barthel
Central Facility for Electron Microscopy (GFE)
RWTH Aachen University
Aachen 52074, Germany

Prof. C.-L. Jia, Dr. C. Lenser, Prof. R. Dittmann
Peter Grünberg Institute
Jülich Research Centre
Jülich 52425, Germany

DOI: 10.1002/adfm.201500852

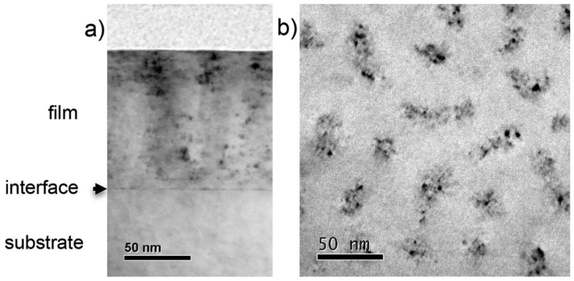

Figure 1. a) Cross-section and b) plan-view BF-TEM images of the Fe-doped $SrTiO_3$ film grown on a Nb-doped $SrTiO_3$ substrate.

Figure 2a,b shows high-resolution cross-section HAADF images recorded along [1 1 0] and [0 1 0] zone axes, respectively. A prominent feature of the cluster areas is that extra atomic columns (open circles) appear in addition to Sr and Ti atomic columns (solid circles). By careful inspection of the relative brightness and position of the extra atomic columns, one can consistently conclude that the appearance of the extra atomic columns is the result of lattice overlapping of the antiphase nanodomains. The antiphase nanodomains have a relative lattice translation vector of $a/2$ [0 1 1] with respect to the surrounding film as sketched in Figure 2c. Because the antiphase nanodomains are a few nanometers in size (Figure 1), it is quite reasonable that they often appear to overlay with the matrix.

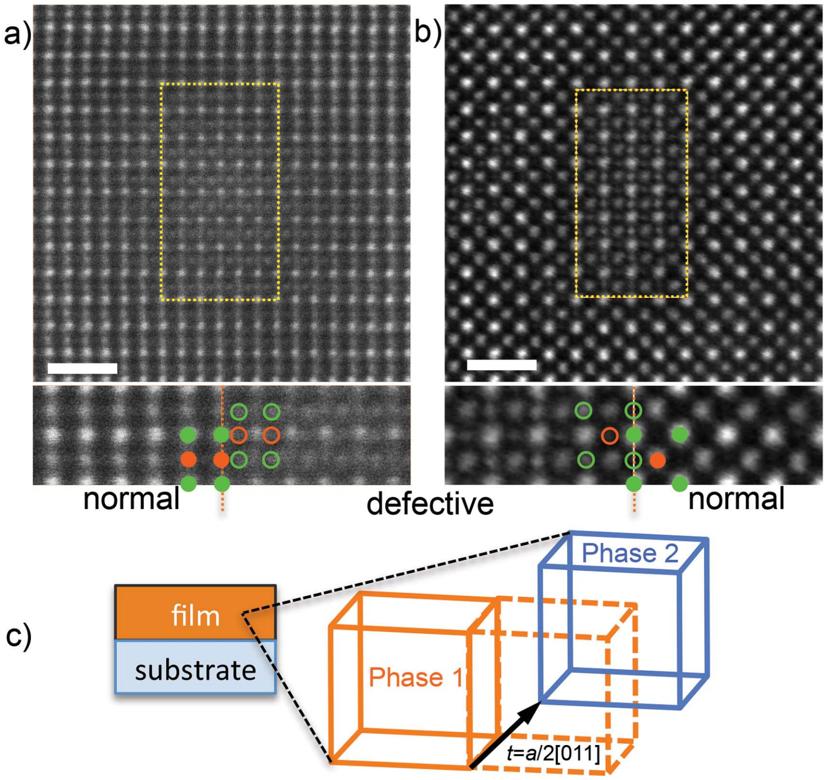

Figure 2. Cross-section HAADF images recorded along a) the [1 1 0] (200 kV) and b) the [0 1 0] (300 kV) zone axis. Most evident defective areas were marked by rectangles and compared with respective normal lattices at the bottom images. Solid circles: matrix lattice; open circles: antiphase lattice (green: Sr, red: Ti). Scale bar: 1.0 nm. c) Schematic illustration of the relative lattice translation vector (black arrow).

Multislice STEM simulations based on the proposed antiphase structure are in remarkable agreement with the experimental results for both [1 1 0] and [0 1 0] zone-axis imaging. The structural models used for simulation were constructed as two layers of $SrTiO_3$ units with a lattice translation of $a/2$ [0 1 1] relative each other. Fe doping was not taken into account in the simulation due to the low doping level of 5.0%, and due to the extremely small HAADF signal difference occurring when exchanging a Ti atom by an Fe atom. The thickness of the top layer was varied within a few nanometers and a few tens of nanometers for the bottom layer. Aberrations were not taken into account in the simulations since this work was not aim to fully quantify the experimental images, but rather to verify the proposed structural model. After subtraction of a respective constant background, the experimental and simulated images were normalized to the same mean intensity for comparison of the image intensity distributions.

Figure 3a shows the representative region of interest in Figure 2a. Because the raw image is quite noisy, it is necessary to remove noise for reliable comparison with multislice simulations. Figure 3b shows a denoised image by averaging and then filtering by a nonlinear filter.[17] By examining the difference between the original and denoised images as shown in Figure 3c, one may see that the processed image essentially represents the original experimental image and thus appears valid as an experimental reference image. An optimum match between simulated and experimental reference images was obtained from a structural model with one domain with a thickness of 1.80 nm overlaying on another with a thickness of 14.78 nm (Figure 3d). The maximum of cross correlation is 0.99, indicating a remarkable similarity. Line profiles along the indexed atomic planes as indicated in Figure 3b further show a surprising agreement between the experimental observations and simulations (Figure 3e).

Moreover, the experimental and simulated results for [0 1 0] zone axis also appear consistent with the proposed antiphase structure. Since the raw image recorded along [0 1 0] zone axis is less noisy (**Figure 4**a), an experimental reference image was obtained by averaging of original experimental image without further filtering (Figure 4b). A simulated image from an antiphase structural model with one domain of 2.73 nm overlaying on another domain of 8.18 nm appears to be in good match with experimental reference image (Figure 4c). The maximum of cross correlation between the simulated and experimental reference images is 0.96. Line profiles also show good agreement of the normalized intensity distributions (Figure 4d). The main difference appears to be that the simulated image shows slightly narrower peaks compared with the experimental reference image, which possibly might be because

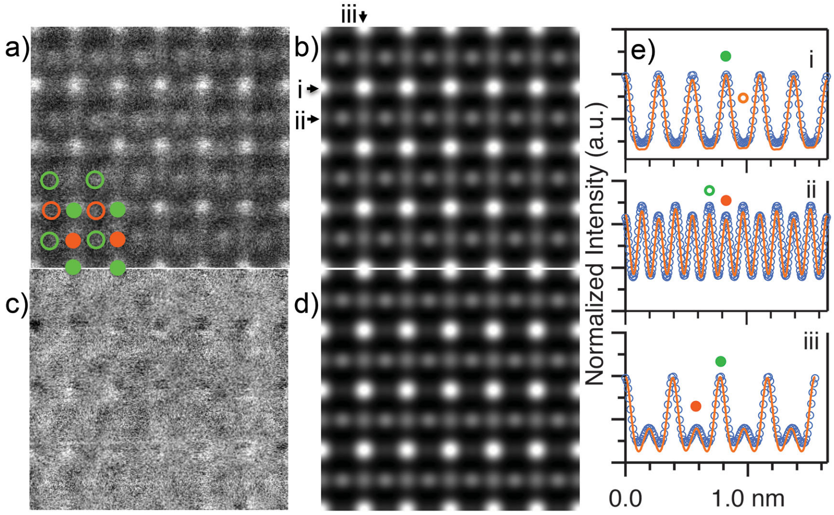

Figure 3. a) Magnified experimental HAADF image of defect area recorded along [1 1 0] zone axis, b) experimental reference image by averaging and filtering, c) residue image by subtraction of (b) from (a), d) multislice simulated image, and e) line profiles alone atomic planes marked in (b), scattered plot: experimental reference, solid line: simulation. Atomic marks, solid circles: matrix lattice; open circles: antiphase lattice (green: Sr, red: Ti).

aberrations such as a small defocus were not taken into account in the simulation.

2.2. Atomic Structure of APBs

In addition to identification of the antiphase nanodomains, it is more important and interesting to reveal the atomic structures of the APBs. Overlapping problems, however, hinder an artifact-free imaging of the atomic structure at the APBs in the cross-section samples. Plan-view samples appear to have less severe overlapping problems but more sever charging problem. To overcome the charging problem a multiple short time exposure (1.0 s frame^{-1}) and iterative rigid alignment method was used. In the iterative rigid alignment, the accumulated sum of aligned images was used as a reference image for aligning the next image in the first iteration. Then the last accumulated sum was used as a reference image for all the images in the next iteration and this process goes iteratively. From the plot of the mean of residual mismatch against the number of alignment iteration (**Figure 5**), one can see that more than five iterations appear to be a rational choice.

Figure 6a shows the atomic resolution plan-view HAADF-STEM image of an antiphase nanodomain with size of 8 × 10 unit cells. The image was averaged from 50 frames with exposure time of 1.0 s frame^{-1} by ten iterations using the iterative rigid alignment method. Strain contrast was minimized by damping the center spots in Fourier space to see all the details of boundaries. Because the z-axis component of the lattice translation vector is not visible in planar view, the observed lattice translation of $a/2$ [0 1 0] across the APBs is consistent with the overall lattice translation of $a/2$ [0 1 1]. The APBs lie mostly in the {1 0 0} planes and partially in the {1 1 0} planes. Three types of APBs at edge-on orientation were labeled in Figure 6a.

There will be two different types of APBs lying in {1 0 0} planes depending on whether they are parallel to the lattice translation vector $t = a/2$ [0 1 1] (type 1) or not (type 2), as illustrated in Figure 6b. **Figure 7**a shows the magnified experimental image of a type 1 APB that clearly resolves the arrangement of the atomic columns. A most striking characteristics of the type 1 APB is that at the boundary the atom columns corresponding to Sr for the left phase (matrix), as marked by dashed-line circle, appear darker than normal Sr columns but show about the same brightness as normal Ti columns. Suppose these atomic columns are Sr columns but with lower occupancies, each of these Sr atoms will occupy a corner of the TiO_6 octahedron from the adjacent right phase (antiphase nanodomain) as illustrated in Figure 7b. This configuration, however, seems not to be a favorable atomic configuration since two positive Sr and Ti cations become very close (from 0.338 to 0.195 nm). A more physically reasonable atomic arrangement appears to be that extra Ti atoms are present at the type 1 APB and occupy centers of oxygen octahedra, in which the six oxygen atoms are equally contributed by the two adjacent domains with TiO terminations, as shown in Figure 7b. Following this idea, the type 1 APB could be formed by three TiO_2 layers composed of edge-sharing

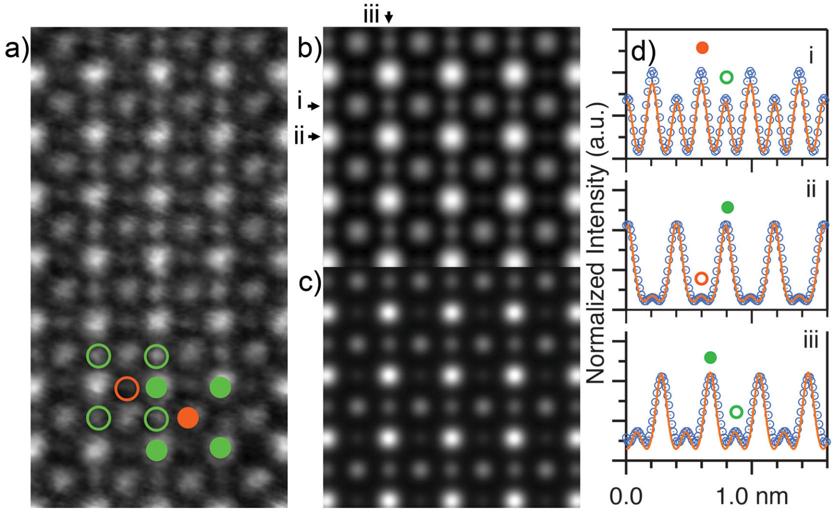

Figure 4. a) Magnified experimental HAADF image of defect area recorded along [0 1 0] zone axis, b) experimental reference image by averaging, c) multislice simulated image, and d) line profiles alone atomic planes marked in (b), scattered plot: experimental reference, solid line: simulation. Atomic marks, solid circles: matrix lattice; open circles: antiphase lattice (green: Sr, red: Ti).

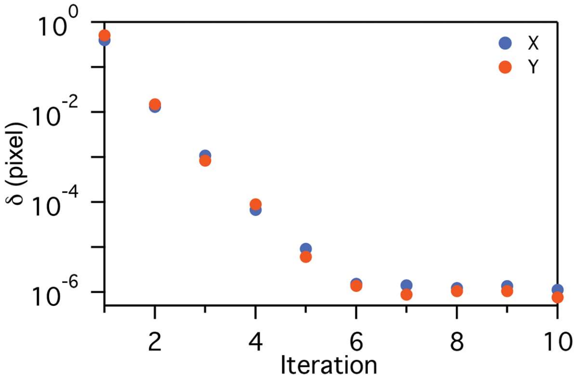

Figure 5. Mean of residual mismatch, δ, against the number of alignment iteration. The values of δ are obtained by averaging the absolute values of the relative shifts between the respective averaged image and individual aligned images.

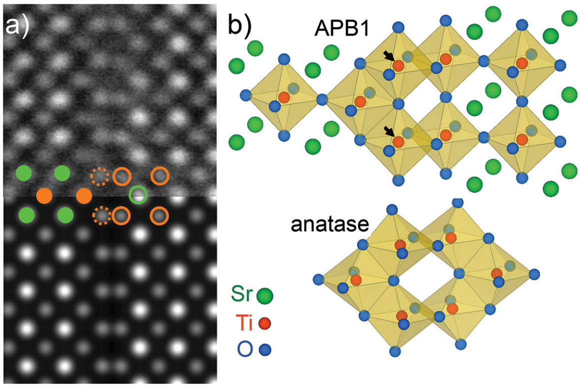

Figure 7. a) Magnified (top) and simulated (bottom) HAADF images of type 1 APB and b) structural models of type 1 APB and TiO_2 anatase. Arrows indicate extra Ti atoms.

TiO_6 octahedra, therefore, with a local Ti enrichment. Such an arrangement of edge-sharing TiO_6 octahedra is commonly seen in TiO_2, such as anatase. Image simulations also support the proposed structural model. As seen in Figure 7a, the simulated STEM image based on the proposed type 1 APB structural model matches the experimental image very well.

Type 2 APB is also found to consist of edge-sharing TiO_6 octahedra, but in a more straightforward way. **Figure 8** shows the magnified experimental HAADF image of type 2 APB. One can clearly see that at the type 2 APB the Ti columns from two adjacent domains appear to be connected to have a relative lattice translation of $a/2$ [0 1 0]. Further, considering the relative lattice translation in the imaging direction of $a/2$ [0 0 1], connecting two TiO-terminated {1 0 0} planes together results in two layers of TiO_2, forming chains of edge-sharing TiO_6 octahedra, as shown in Figure 8. The corresponding simulated image based on the proposed structural model is in good agreement with the experimental image, as seen in Figure 8.

The magnified HAADF image of the observed APB lying on {1 1 0} planes (type 3) is shown in **Figure 9** with a very distinct staircase-like feature. The atomic structure of the type 3 APB may be considered as a combination of type 1 and 2 APBs. Chains of edge-sharing TiO_6 octahedra appear with the presence of extra Ti atoms. Details of the atomic structure of type 3 APB are schematically shown in Figure 9. The image simulations based on the structural model lead a good match with the observed distinct staircase-like feature.

The above results and discussions show that all the three types of APBs have edge-sharing TiO_6 octahedral chains and are of local Ti-enrichment. The existence of edge-sharing feature for TiO_6 octahedra can be considered to provide the flexibility for changing their directions, thus for forming enclosed antiphase nanodomains. Since antiphase nanodomains were not observed in Fe-doped $SrTiO_3$ single crystals, the formation of antiphase nanodomains should be related to the PLD growth process. A reasonable explanation appears to be atomic scale chemical inhomogeneities or fluctuations during the film growth, which in turn induce the formation of antiphase nanodomains. It is important, however, to point out that we should not rule out that the inhomogeneity also occurs for Fe. Further efforts are in process to overcome the charging problem in the plan-view samples to obtain conclusive direct chemical measurements by

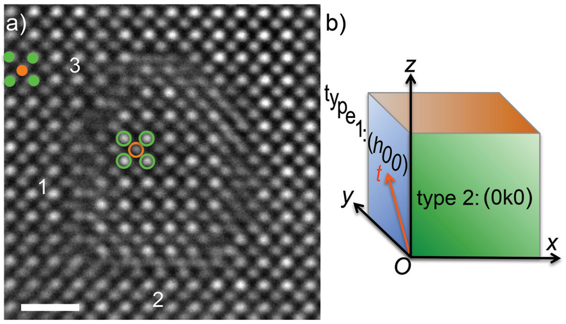

Figure 6. a) Plan-view HAADF image recorded along the [0 0 1] zone axe (80 kV, averaged from 50 frames with exposure time of 1.0 s $frame^{-1}$ by ten iterations using an iterative rigid alignment method, strain contrast was minimized by damping the center spots in Fourier space), three types of edge-on APBs were labeled, scale bar: 1.0 nm and b) a schematic of the relationship between the lattice translation vector $t = a/2$ [0 1 1] and two different types of APBs lying in {1 0 0} planes.

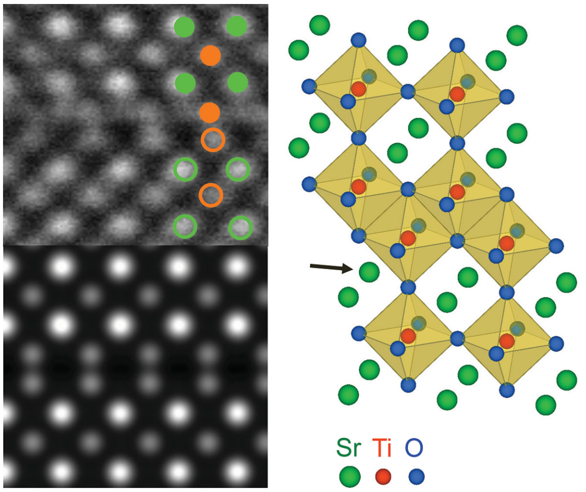

Figure 8. Type 2 APB, top: magnified HAADF image, bottom: simulated image, and right: structural model, the arrow indicates the electron beam direction.

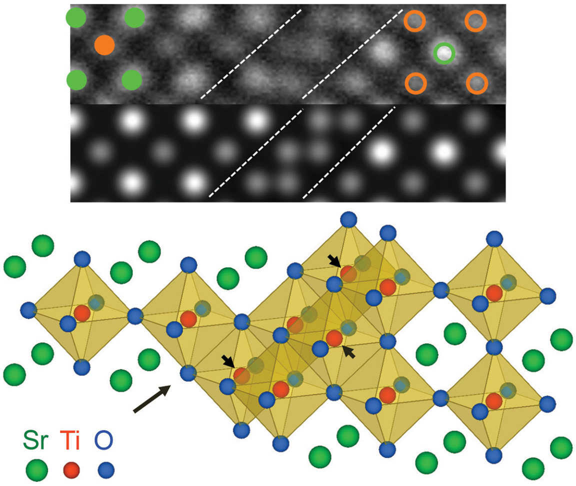

Figure 9. Type 3 APB, top: magnified HAADF image, middle: simulated image, and bottom: structural model. The staircase-like features were highlighted between doted lines. Extra Ti atoms were marked by short arrows. Long arrows indicate the electron beam direction.

such as electron energy-loss spectroscopy (EELS) and energy dispersive X-ray spectroscopy (EDS) imaging.

3. Conclusion

In summary, our study has revealed the atomic structures of antiphase nanodomains in Fe-doped $SrTiO_3$ films grown by PLD technique. The crystallographic translation vector between the matrix and the antiphase nanodomain is $a/2$ [0 1 1], being distinct from $a/2$ [1 1 1] of RP type APBs. Moreover, in contrast to RP type APBs having a local Sr-enrichment, the prominent result is that all the three types of APBs of the antiphase nanodomains appear to consist of edge-sharing TiO_6 octahedral chains with a local Ti enrichment. Since defects play an essential role in many functional properties in perovskites, such as the resistive switching processes in $SrTiO_3$, the identified atomic structures of these defects provide the structural basis for theoretical calculations for thoroughly understanding their properties. Moreover, our results show the possibility toward rational growth of antiphase nanodomains in other perovskite oxides by precise control of chemical stoichiometry, which may in turn offer opportunities to rationally tailoring their functional properties.

4. Experimental Section

$SrTi_{0.95}Fe_{0.05}O_3$ thin films were grown by PLD using a KrF excimer laser with a wavelength of 248 nm at a frequency of 5 Hz. Films were grown on (0 0 1)-oriented 1.0 at% Nb-doped $SrTiO_3$ substrates (Crystec, Berlin, Germany) at a substrate temperature of 700 °C, an O_2 pressure of 0.25 mbar, and a laser fluence of 0.8 J cm^{-2} at the target. The as-grown films were cooled to room temperature in 500 mbar of O_2. The obtained films have a thickness of ≈100 nm. Plan-view specimens were prepared by a standard procedure including grinding, dimpling, and final ion-beam milling in a stage cooled with liquid nitrogen. Cross-sectional lamellae were prepared by focus ion beam using an FEI Helios NanoLab 400S (FEI Company, Hillsboro, OR, USA). The lamellae were further thinned by a Bal-Tec Res-120 system (Bal-Tec AG, Fuerstentum Liechtenstein, Germany) and finally cleaned by a Fischione Nanomill 1040 system (E.A. Fischione Instruments, Inc., Export, PA, USA). The TEM imaging was performed with an image C_S-corrected FEI Titan 80-300 microscope operated at 300 kV accelerating voltage. The atomic-resolution HAADF-STEM imaging was carried out with an FEI Titan^3 50-300 PICO microscope equipped with a high-brightness field emission gun, a monochromator, a probe C_S corrector, and a C_S–C_C (chromatic aberration) achro-aplanat image corrector. Multislice HAADF-STEM image simulations were performed using the Dr. Probe software.[18] Structural models were visualized with VESTA.[19]

Acknowledgements

This work was supported by the Deutsche Forschungsgemeinschaft (SFB 917). The authors thank Cong Zhang for providing the single crystal samples, Doris Meertens, Wilma Sybertz, and Maximilian Kruth for preparing the TEM lamellae, Lothar Houben and Chris Boothroyd for training in operating the PICO microscope, and Lei Jin for helpful discussion. The authors are also especially grateful to Rafal Dunin-Borkowski for reading the manuscript and providing insightful comments.

Received: March 3, 2015

---

[1] J. G. Bednorz, K. A. Müller, *Z. Phys. B: Condens. Matter* **1986**, *64*, 189.
[2] A. P. Ramirez, *J. Phys. Condens. Matter* **1997**, *9*, 8171.
[3] A. Ohtomo, H. Y. Hwang, *Nature* **2004**, *427*, 423.
[4] J. H. Haeni, P. Irvin, W. Chang, R. Uecker, P. Reiche, Y. L. Li, S. Choudhury, W. Tian, M. E. Hawley, B. Craigo, A. K. Tagantsev, X. Q. Pan, S. K. Streiffer, L. Q. Chen, S. W. Kirchoefer, J. Levy, D. G. Schlom, *Nature* **2004**, *430*, 758.
[5] R. Waser, M. Aono, *Nat. Mater.* **2007**, *6*, 833.
[6] R. Merkle, J. Maier, *Angew. Chem. Int. Ed.* **2008**, *47*, 3874.
[7] R. Waser, R. Dittmann, G. Staikov, K. Szot, *Adv. Mater.* **2009**, *21*, 2632.
[8] D. J. Keeble, S. Wicklein, L. Jin, C. L. Jia, W. Egger, R. Dittmann, *Phys. Rev. B* **2013**, *87*, 195409.
[9] T. Ohnishi, M. Lippmaa, T. Yamamoto, S. Meguro, H. Koinuma, *Appl. Phys. Lett.* **2005**, *87*, 241919.
[10] C. Xu, S. Wicklein, A. Sambri, S. Amoruso, M. Moors, R. Dittmann, *J. Phys. Appl. Phys.* **2014**, *47*, 034009.
[11] C. M. Brooks, L. F. Kourkoutis, T. Heeg, J. Schubert, D. A. Muller, D. G. Schlom, *Appl. Phys. Lett.* **2009**, *94*, 162905.
[12] Y. Tokuda, S. Kobayashi, T. Ohnishi, T. Mizoguchi, N. Shibata, Y. Ikuhara, T. Yamamoto, *Appl. Phys. Lett.* **2011**, *99*, 173109.
[13] A. Koehl, D. Kajewski, J. Kubacki, C. Lenser, R. Dittmann, P. Meuffels, K. Szot, R. Waser, J. Szade, *Phys. Chem. Chem. Phys.* **2013**, *15*, 8311.
[14] T. Suzuki, Y. Nishi, M. Fujimoto, *Philos. Mag. A* **2000**, *80*, 621.
[15] T. Ohnishi, K. Shibuya, T. Yamamoto, M. Lippmaa, *J. Appl. Phys.* **2008**, *103*, 103703.
[16] J. S. Jeong, P. Ambwani, B. Jalan, C. Leighton, K. A. Mkhoyan, *ACS Nano* **2013**, *7*, 4487.
[17] H. Du, *Ultramicroscopy* **2015**, *151*, 62.
[18] J. Barthel, Dr. Probe-STEM simulation software, http://www.er-c.org/barthel/drprobe/ (accessed: September, **2013**).
[19] K. Momma, F. Izumi, *J. Appl. Crystallogr.* **2011**, *44*, 1272.